nature photonics

Article

https://doi.org/10.1038/s41566-025-01763-5

Observation of quantized vortex in atomic Bose–Einstein condensate at Dirac point with emergent spin–orbit coupling

Received: 10 January 2025

Accepted: 21 August 2025

Published online: 29 September 2025

Check for updates

Yunda Li[1,4], Wei Han[1,4], Zengming Meng[1,4], Wenxin Yang[1], Cheng Chin[2] ✉ & Jing Zhang[1,3] ✉

The degeneracy of two or more energy bands at a singular point in the band structure, such as a Dirac point, gives rise to intriguing quantum phenomena as well as unusual material properties. Systems at the Dirac points can possess topological charges and their unique properties can be probed by various methods, such as transport measurement, interferometry and momentum spectroscopy. While the topology of Dirac point in the momentum space is well studied theoretically, observation of topological defects in a many-body quantum system at Dirac point remains an elusive goal. Based on atomic Bose–Einstein condensate in a graphene-like optical honeycomb lattice, we directly observe emergence of quantized vortices induced by the non-commutativity between the harmonic trap and the pseudo-spin–orbit coupling at the Dirac point. By adiabatic control of the honeycomb lattice with an additional harmonic trapping potential, the phase diagram of lattice bosons at the Dirac point is revealed. Our work provides a new way of generating vortices in a quantum gas, and the method is generic and can be applied to different types of optical lattices with topological singularities, including topological flat bands near Dirac points in twisted bilayer optical lattices.

Materials with gapless excitations such as semimetals[1,2] have attracted a great deal of interest in the past decade. A prominent example is graphene[3,4], where a honeycomb lattice of carbon atoms supports singular Dirac points near which the energy dispersion is linear. The presence of singularity in momentum space leads to remarkable phenomena, such as trembling motion (Zitterbewegung)[5,6], Klein paradox[7], electron chirality and anomalous quantum Hall effect[8]. The extraordinary properties of graphene near the Dirac point have motivated great interest to quantum simulate graphene based on electrons, photons and cold atoms[9].

Quantum physics at the Dirac points has been investigated in photonic crystal systems. Dirac points in photonic graphene offer a unique way to generate optical vortices (optical beam carrying orbital angular momenta) by transforming pseudo-spin winding in momentum space into phase winding of the optical beam in real space[10–12]. In quantum gases, the optical honeycomb lattice has also been realized experimentally[13,14], and the Dirac point and global topology can be determined by the evolution of quantum states via transporting wave packets[15–17], and momentum-resolved tomography[18–22]. In these systems a Dirac point can be identified when atoms encircles or passes through the singularity[15–17]. However, the direct observation of quantized vortices or topological defects emerging at the Dirac point in a quantum gas remains elusive.

The conventional method for generating vortices near the Dirac point, such as those used to create optical vortices in photonic graphene[11,12], is based on a dynamic process involving coherent pseudo-spin flips. The initial state is prepared in the pseudo-spin up

[1]State Key Laboratory of Quantum Optics Technologies and Devices, Institute of Opto-Electronics, Collaborative Innovation Center of Extreme Optics, Shanxi University, Taiyuan, People's Republic of China. [2]James Franck Institute, Enrico Fermi Institute, Department of Physics, University of Chicago, Chicago, Illinois, USA. [3]Hefei National Laboratory, Hefei, People's Republic of China. [4]These authors contributed equally: Yunda Li, Wei Han, Zengming Meng. ✉e-mail: cchin@uchicago.edu; jzhang74@sxu.edu.cn

https://doi.org/10.1038/s41566-025-01763-5

(or pseudo-spin down) component at the Dirac point. The spin is then flipped in the evolution, which generates a spin down (or spin up) component that carries a quantized vortex with topological charge $l = +1$ (or $l = -1$) (Supplementary Fig. 5).

Here, we develop a new method for generating quantized vortices at the Dirac point by adiabatic control of a honeycomb lattice with an additional harmonic trapping potential. While a harmonic trap is typically present in cold-atom optical lattice experiments[14–18], it usually serves only to confine the atoms. In our experiment, however, the harmonic trap plays a essential role in vortex formation. Its non-commutativity with the pseudo-spin–orbit coupling near the Dirac point gives rise to a momentum-dependent gauge potential, which induces an angular superfluid velocity and finite vorticity, as well as an effective centrifugal potential around the Dirac point, ultimately leading to the emergence of vortices in momentum space. The developed method relies on the adiabatic evolution of atoms, a feature unique to ultracold atom systems, which offers tunable parameters for exploring quantum phase transitions. We demonstrate that tuning the harmonic trapping frequency and the optical lattice depth enables full control over distinct quantum phases, including superfluid, Mott insulator, and vortex phases.

We observe quantized vortex generation in a Bose–Einstein condensate (BEC) of Rubidium-87 (^{87}Rb) atoms prepared at the Dirac point of a two-dimensional graphene-like honeycomb lattice. The Hamiltonian of the system can be expressed in the Rashba spin–orbit coupling form with $H_R = (k_y\sigma_x - k_x\sigma_y)v_0 \equiv \Omega\sigma_- + \Omega^*\sigma_+$, where $(k_x, k_y) = (k\cos\theta, k\sin\theta)$ is the momentum operator, $\sigma_{x,y}$ are Pauli matrices, $v_0 = \hbar^2 k_0/2m$ is the spin–orbit coupling strength, m is the atomic mass, $\hbar$ is the reduced Planck constant, $k_0 = 2\pi/\lambda$ is the photon recoil momentum of the lattice beam at wavelength λ, $\Omega = -\mathrm{i}ke^{i\theta}v_0$, and $\sigma_\pm = (\sigma_x \pm i\sigma_y)/2$ are the spin raising/lowering operators. The momentum dependence of Ω implies that a spin flip is necessarily accompanied by the generation of a vortex phase, as illustrated in Fig. 1a. Moreover, the eigenstates also exhibit a vortex structure around the Dirac point, as shown in Fig. 1b,c.

We create the optical honeycomb lattice by interfering three red-detuned laser beams operating at wavelength $\lambda = 820$ nm. The beams propagate within the x–y plane and intersect at an angle $\xi = 120°$ with linear polarizations in the x–y plane, as shown in Fig. 2a. A homogeneous magnetic bias field $B_0 = 2.7$ G is applied in the x axis, which defines the quantization axis. The interference of the laser beams leads to an attractive scalar lattice potential on the atoms[19,23]. The natural momentum and energy units of the lattice are the recoil momentum $\hbar k_R$ and the recoil energy $E_R = \hbar^2 k_R^2/2m = h \times 2.56$ kHz, where $k_R = k_0 \sin(\xi/2)$ is the lattice momentum. The lowest two energy bands of the honeycomb lattice exhibit Dirac points with linear dispersion, as shown in Fig. 2c,d.

The atoms are initially prepared in the spin state $|F = 1, m_F = 1\rangle$. The sample is confined to a single layer of an accordion lattice along the z direction (gravity direction) and subjected to a harmonic trap in the x–y plane. Then the atoms are loaded into the lowest Bloch band at the Γ_0 point by adiabatically ramping up the honeycomb lattice. Subsequently, the honeycomb lattice potential is smoothly accelerated to a velocity $\mathbf{v}$. The low acceleration ensures that the atoms remain in the lowest band with zero quasi-momentum in the laboratory frame while the atoms evolve adiabatically into the quasi-momentum $\mathbf{q} = -m\mathbf{v}/\hbar$ in the lattice frame. Throughout both the loading and acceleration processes, the harmonic trapping frequency ω_{xy} remains unchanged. Finally, the harmonic trapping potential is ramped off quickly within 0.2 ms, followed by simultaneous switching off the honeycomb lattice and accordion lattice, after which time-of-flight (TOF) imaging is performed. The timing sequence is shown in Fig. 2b. Here we control the lattice velocity $\mathbf{v}_i$ by detuning the i-th lattice beam according to $\mathbf{v}_i = a\Delta\omega_i\hat{k}_i$, where $a = 2\lambda/3$ is lattice constant and $\hat{k}_i$ is the unit vector in the propagating direction of the i-th laser beam that forms the honeycomb lattice.

In order to create a quantized vortex at the Dirac point, we transfer the BEC adiabatically from the ground state Γ_0 to Dirac point K_0.

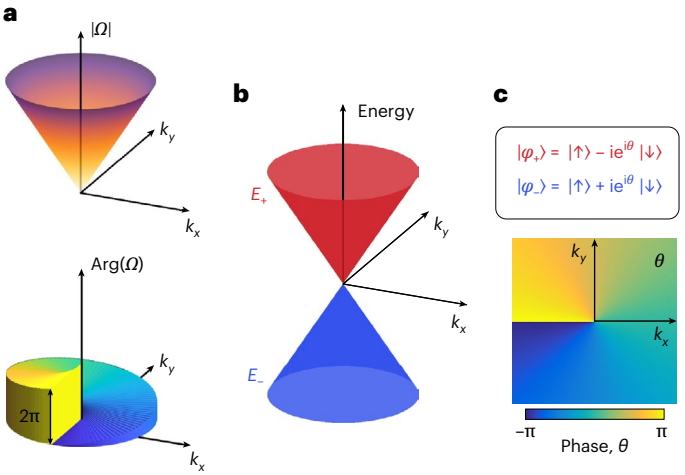

Fig. 1 | Quantized vortex state at Dirac point. a, Amplitude and phase of the pseudo-spin–orbit coupling parameter $\Omega = -\mathrm{i}ke^{i\theta}v_0$ from the Dirac Hamiltonian $H_R = (k_y\sigma_x - k_x\sigma_y)v_0 = \Omega\sigma_- + \Omega^*\sigma_+$. **b**, Energy band near the Dirac point. The eigenenergies $E_\pm = \pm v_0 k$ of the Dirac Hamiltonian correspond to the upper and lower branches (labelled with red and blue colour), respectively. **c**, Eigenstates $\varphi_\pm$ corresponding to eigenenergies $E_\pm$. The eigenstates exhibit a vortex phase with topological charge $l = +1$ around the Dirac point.

Since the Dirac point is not the ground state of the system, the BECs have a limited lifetime of several milliseconds (Extended Data Fig. 1). The lifetime is, however, sufficient since the BEC can be adiabatically transferred from Γ_0 to K_0 within 0.8 ms. At the same time, we introduce a harmonic trapping potential in x–y direction, and then map the momentum distribution of the BEC based on TOF imaging. Here the harmonic trapping potential is critical for the formation of vortex, as it does not commute with the pseudo-spin–orbit coupling and thus induces a gauge potential at the Dirac point (Supplemental Section 1).

We map out the entire first Brillouin zone $n = 1$, including the six Dirac points $^{(a)}K_0$ and $^{(a)}K_0'$, $(a = 1, 2, 3)$, see Fig. 3a, which connect to the second energy bands $n = 2$ as shown in Fig. 2d. In TOF images, the vortex structure manifests in the density distribution of the three distinct momentum components when the BEC is located at the Dirac points of the first Brillouin zone; see the enlarged image of Fig. 3a.

The vortex formation can be attributed to the emergent spin–orbit coupling near the Dirac point (Supplementary Section 1). To describe the BEC near the Dirac points K_0 (K_0') of the lowest band, we set the frequency detunings of the lattice beams as $\Delta\omega_2 = \pm 4E_R/\hbar$ (+ for K_0 and − for K_0'). This condition corresponds to the two-photon Bragg transition frequency ω_B between lattice beams 2 and 1 (3). The quadratic energy-momentum dispersion of the massive atoms defines a unique energy difference with $\omega_B = 4E_R/\hbar$, which just matches the stimulated two-photon Bragg transition frequency. In this case, the three momentum components of the atoms at $^{(1)}K_0$, $^{(2)}K_0$ and $^{(3)}K_0$ are resonantly coupled, and the effective Hamiltonian shows three modes with pair-wise couplings, which in the dressed state basis is given by

$$H_{\mathrm{eff}} = \frac{\hbar^2 k_0}{2m}\begin{pmatrix} 0 & k_y + \mathrm{i}k_x & k_y - \mathrm{i}k_x \\ k_y - \mathrm{i}k_x & 0 & k_y + \mathrm{i}k_x \\ k_y + \mathrm{i}k_x & k_y - \mathrm{i}k_x & 0 \end{pmatrix} + \begin{pmatrix} -\Lambda & 0 & 0 \\ 0 & -\Lambda & 0 \\ 0 & 0 & 2\Lambda \end{pmatrix}, \quad (1)$$

https://doi.org/10.1038/s41566-025-01763-5

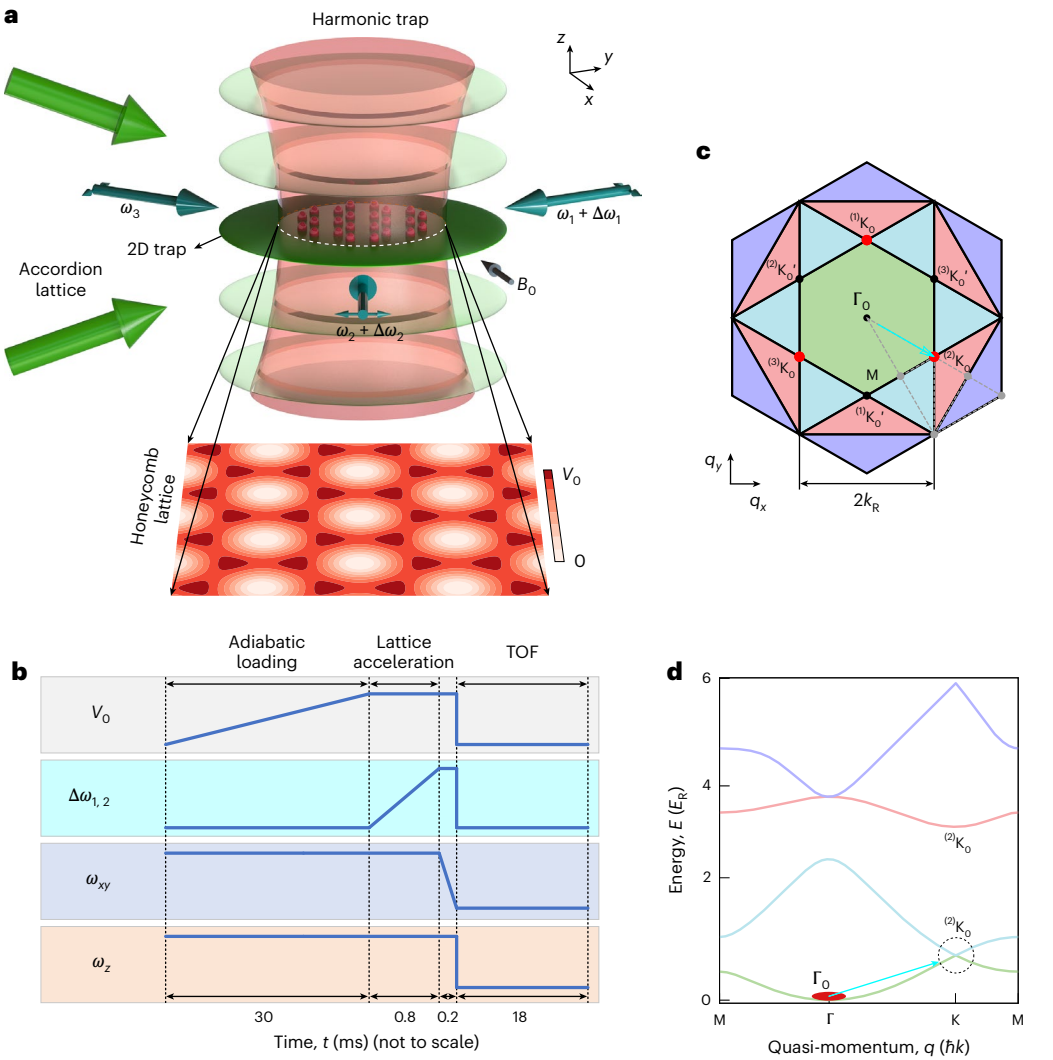

Fig. 2 | Experimental scheme. a, The BEC is confined to a single layer of two-dimensional (2D) pancakes by an accordion lattice. A far red-detuned 1064 nm laser beam propagating along the *z* axis provides a harmonic trapping potential in the *xy* plane. A honeycomb lattice is formed by interfering three laser beams in the *xy* plane at 120° angles, with their propagation directions indicated by dark cyan single arrows and their in-plane linear polarizations indicated by dark cyan double arrows. A homogeneous magnetic field B_0 is applied along the *x* direction. **b**, Experimental sequence showing the ramp profiles of the lattice depth V_0, detuning $\Delta\omega_{1,2}$, harmonic trapping frequency ω_{xy} and accordion lattice intensity corresponding to the axial trapping frequency ω_z. **c**, The first four Brillouin zones of the lattice are presented with green, cyan, pink and purple, respectively. Dirac points in the first Brillouin zone are labelled as $^{(a)}K_0$ or $^{(a)}K_0'$, where $a = 1, 2, 3$. The dashed lines indicate the high symmetry paths for the band structure of **d**. **d**, The energy bands of the honeycomb lattice with the lattice depth $12\,E_R$. The colours of energy bands correspond to those in panel **c**. A Dirac point occurs at K_0 (dashed circle), where the lowest two bands touch linearly, and can be described by the model presented in Fig. 1. In our experiment, the condensate (red ellipse) is initially prepared in the lowest state Γ_0 and then quenched to the Dirac point at $^{(2)}K_0$, indicated by the cyan arrow.

where Λ is the pair-wise coupling strength and proportional to the lattice depth. This Hamiltonian resembles the ring scheme of three cyclically Raman coupled ground hyperfine spin states[24–26]. The dressed-state basis $\Psi(\mathbf{k})$ is connected to the bare-state basis $\Psi(\mathbf{k}) = \{|^{(1)}K_0 + \mathbf{k}\rangle, |^{(2)}K_0 + \mathbf{k}\rangle, |^{(3)}K_0 + \mathbf{k}\rangle\}$through a unitary transformation

$$S = \frac{1}{\sqrt{3}}\begin{pmatrix} 1 & 1 & 1 \\ e^{i\frac{2\pi}{3}} & e^{-i\frac{2\pi}{3}} & 1 \\ e^{-i\frac{2\pi}{3}} & e^{i\frac{2\pi}{3}} & 1 \end{pmatrix}. \quad (2)$$

This effective Hamiltonian very well describes the $n = 1, 2, 3$ Bloch bands near K_0 and the singular Dirac degeneracy between the $n = 1$ and $n = 2$ bands (Supplementary Fig. 2). The highest energy band has a much higher energy 3Λ than the lower two bands in equation (1). In an adiabatic process, we can neglect amplitude in the highest energy band and consider only atoms in the lowest two dressed states near the degeneracy. Thus a pseudo-spin 1/2 Hamiltonian with the Rashba pseudo-spin–orbit coupling becomes a very good approximation near the Dirac point and yields the linear dispersion. On the other hand, an effective Hamiltonian with the Dresselhaus spin–orbit coupling with opposite sign of topological charge describes the linear Dirac equation near K_0'; see Supplementary Section 1.

When the BEC is accelerated adiabatically from Γ_0 to K_0 (K_0'), with an appropriate harmonic trapping frequency and optical lattice depth, the condensate is prepared at the spin eigenstate $\psi_s = (1, -ie^{\pm i\theta})^T$ in the pseudo-spin 1/2 representation ($+\theta$ for K_0 and $-\theta$ for K_0'), which is composed of a phase trivial spin up component and a phase nontrivial spin down component. In this case, a quantum vortex with an orbital angular momenta of $\pm\hbar$ is naturally created (Supplementary Section 2).

https://doi.org/10.1038/s41566-025-01763-5

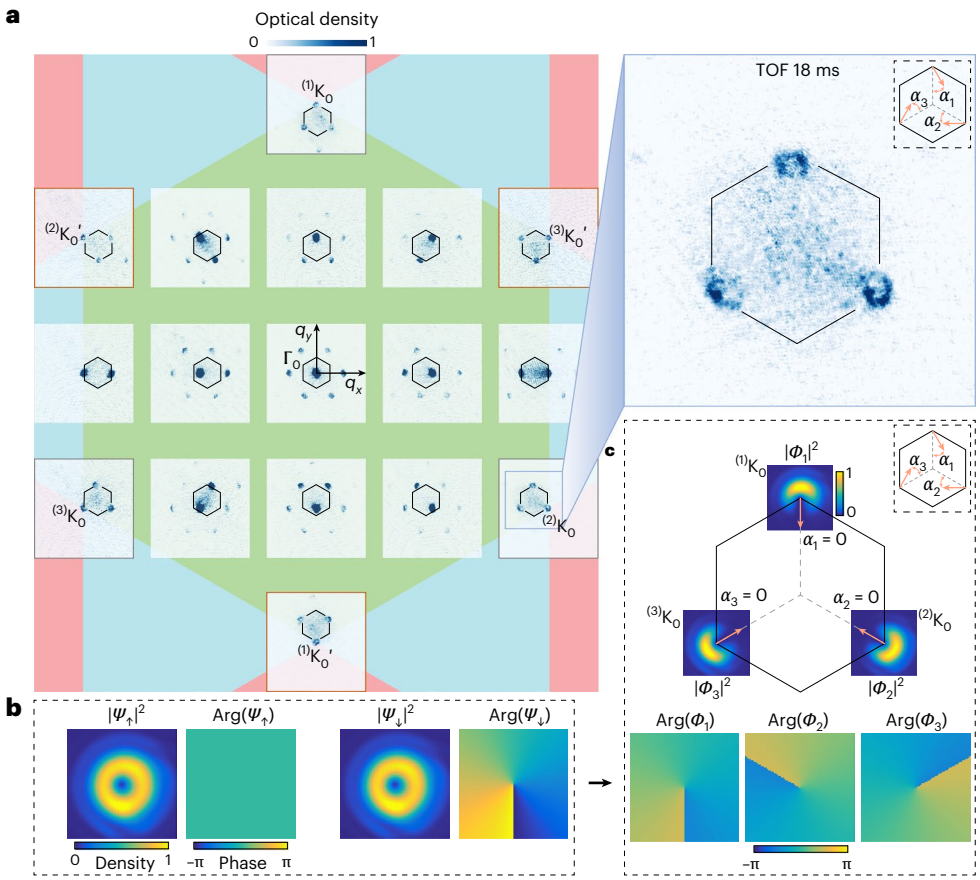

Fig. 3 | Observation of vortex in a Bose–Einstein condensate at Dirac point. **a**, Time-of-flight images of BECs at different quasi-momentum states. Initially prepared in the ground state Γ_0, the BECs are adiabatically transferred to various states, including the six Dirac points at the corners of the first Brillioun zone where vortex emerges. The filling colours of the Brillouin zones are consistent with those in Fig. 2c. The centres of the TOF image panels are pinned at the positions of Brillouin zone where the BECs are prepared. The small hexagon in each panel labels the first Brillouin zone boundary in the atomic momentum distribution. The magnified image details the vortex structure of the BECs with the topological charge $l = +1$. Here BEC is projected to three momentum components ${}^{(1)}\mathrm{K}_0$, ${}^{(2)}\mathrm{K}_0$ and ${}^{(3)}\mathrm{K}_0$ during the TOF expansion. The image shows a directional opening $\alpha_a = 0$ ($a = 1, 2, 3$), which comes from the interference between two pseudo-spin components $\boldsymbol{\psi}_\uparrow$ and $\boldsymbol{\psi}_\downarrow$ of the generated state; see Supplementary Section 2. The depth of optical lattice is 12 E_R and the harmonic trapping frequency in the x–y direction is $2\pi \times 40$ Hz. **b**, Calculated atomic density and phase of the pseudo-spin components $\psi_\uparrow$ and $\psi_\downarrow$ of the generated state for a BEC transferred to the Dirac point K_0. **c**, Calculated three projections of the BEC at Dirac point $\phi_a(k) = \langle {}^{(a)}\mathrm{K}_0 + k\,|\psi\rangle$ relative to the momenta ${}^{(a)}\mathrm{K}_0$. The projections describe the magnified TOF image of (a) and are connected to the quasi-spin components of the generated state as $\phi_1 = \frac{1}{\sqrt{3}}(\psi_\uparrow + \psi_\downarrow)$, $\phi_2 = \frac{1}{\sqrt{3}}\left(e^{i\frac{2\pi}{3}}\psi_\uparrow + e^{-i\frac{2\pi}{3}}\psi_\downarrow\right)$ and $\phi_3 = \frac{1}{\sqrt{3}}\left(e^{-i\frac{2\pi}{3}}\psi_\uparrow + e^{i\frac{2\pi}{3}}\psi_\downarrow\right)$.

We observe the vortex of BECs at the Dirac point based on TOF images. The quantized vortex is observed in three momentum components with triangular configuration locating at the Dirac points of the first Brillouin zone as shown in the magnified image of Fig. 3a. We can see that the quantized vortex is off-centre in the bare state representation due to the interference between two spin dressed states. Note that one of two spin dressed states has the phase singularities $e^{i\theta}$ for K_0 and the other is trivial; see Fig. 3b. The off-centre atomic density distribution in the bare-state basis for K_0 acquires a directional opening with an angle $\alpha = 0$, see Fig. 3c, where the angle α is defined relative to the axis pointing to the centre of the Brillouin zone. The experimental result is in excellent agreement with our theoretical calculation. Although K_0 and K_0' have opposite signs of the topological charges, the atomic density distribution in the bare-state basis for K_0' has the same directional opening with $\alpha = 0$ but different momentum components.

We can transfer BECs from Γ_0 to an any arbitrary quasi-momentum state and obtain the information of the momentum components of the high-symmetry K and M. For example, M point is characterized by two momentum components. Especially, we have identified the singularity of all the six Dirac points ${}^{(a)}\mathrm{K}_0$ and ${}^{(a)}\mathrm{K}_0'$ with $a = 1, 2, 3$ at the corners of the first Brillioun zone by the emergence of quantum vortex. Three distinct momentum components with triangular configuration for K_0 are located at three Dirac points of the first Brillouin zone in the lattice frame, and those for K_0' are located at another three Dirac points, as shown in Fig. 3a.

Near the Dirac point we also observe quantum phase transition based on two controllable parameters. Our system includes a pair of non-commutative interactions: the harmonic potential and the pseudo-spin–orbit coupling. Moreover this system is also described by the Bose–Hubbard model, which permits a quantum phase transition from superfluid (SF) to Mott insulator (MI) as the depth of optical lattices increases. Thus the two controllable parameters: optical lattice depth and the harmonic trapping potential in the x–y direction can induce quantum phase transitions. When we maintain the time sequence of ramping the optical honeycomb lattice and the harmonic trapping laser in x–y direction, three distinct quantum phases are expected, including regular SF, SF with a vortex, and MI; see Fig. 4a.

The TOF images were captured along two paths of the phase diagram: one corresponds to varying harmonic trapping frequencies at a fixed lattice depth of 10.7 E_R (Fig. 4b), and the other corresponds to varying

https://doi.org/10.1038/s41566-025-01763-5

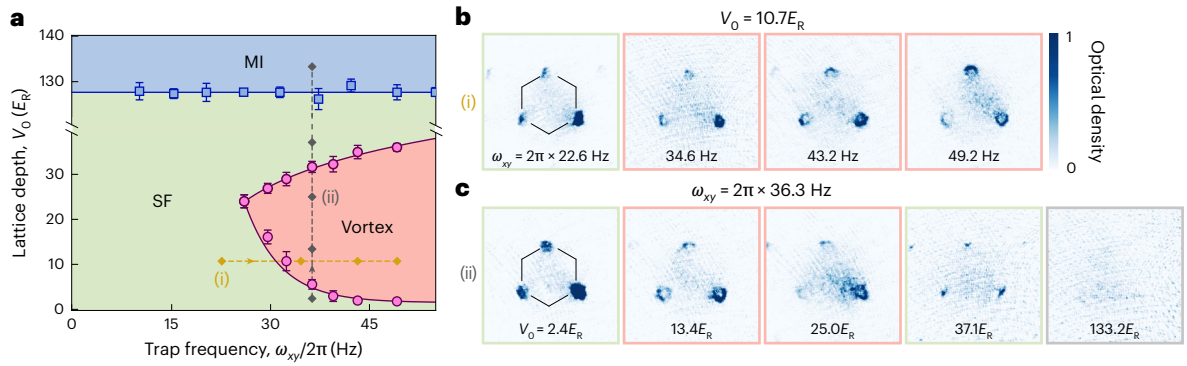

Fig. 4 | Quantum phases of Bose gases at the Dirac point of a honeycomb optical lattice. a, Phase diagram for different trap frequencies ω_{xy} and lattice depth V_0. Here SF and MI refer to superfluid (green) and Mott insulator (blue), respectively. The red area is the region where vortices form in the SF. The magenta and blue points represent mean values from five and three independent measurements, respectively, and the error bars indicate standard deviations of the measured phase boundary positions. Solid lines represent fits to the data using the mean values as a guide. For comparison, theoretical calculation of the phase diagram is shown in the Supplementary Fig. 4. **b**, Examples of images along the line (i) with fixed lattice depth of $V_0 = 10.7\,E_R$ and increasing harmonic trapping frequencies in the x–y. **c**, Images along the line (ii) with fixed harmonic trapping frequency $\omega_{xy} = 2\pi \times 36.3$ Hz and increasing lattice depths. Colour frames of the images from both panels **b** and **c** show assignment of the quantum phase according to the colour code in panel **a**.

lattice depths at a fixed trapping frequency of $2\pi \times 36.3$ Hz (Fig. 4c). We observe no quantized vortex in a weak harmonic trap or in a deep lattice. Moreover, we find that the hole of quantized vortex becomes clearer and its size is larger when increase harmonic trapping potential in x–y direction. This can be understood by noting that, while the harmonic trapping potential confines atoms in real space, its non-commutativity with the pseudo-spin–orbit coupling near the Dirac point induces an effective centrifugal potential in momentum space, given by $m\omega_{xy}^2/8k^2$. This centrifugal potential repels atoms from the Dirac point, resulting in an enlarged vortex core at higher trap frequencies (Supplementary equation (25) and Supplementary Fig. 4). For deeper lattice, the atoms enter the MI region with no superfluid component due to the strong interaction and so there is no quantized vortex of matter wave.

To summarize, our research presents a novel scheme to probe quantum many-body systems with gauge field based on ultracold atoms prepared near the Dirac point. Quantized vortices of BEC generated by the Dirac singular point in momentum space is observed. This method does not involve any chirality or a winding structure in real space and thus position alignment is not required. The uniqueness of our scheme lies in the precise preparation of vortex states at the Dirac point by exploiting the non-commutativity between the harmonic trapping potential and pseudo-spin–orbit coupling. This mechanism clearly goes beyond typical cold-atom optical lattice experiments, where the harmonic potential is usually employed solely for atom confinement and does not actively participate in topological state preparation. From this perspective, our scheme enables the controlled preparation of quantum many-body topological states at band singularities, thereby opening the door to exploring the intriguing interplay among topology, quantum degeneracy, and interactions based on cold atoms.

Applying our method to other lattice geometries will offer access to exotic topological objects, such as higher-order vortices and Dirac monopole at 3D Weyl point. In addition to the vortex density distribution, it is also of great interest to directly probe the vortex phase structure, including the number and sign of the topological charges, by developing phase-sensitive detection techniques in future experiments. In recent years, the twisted bilayer-graphene has attracted broad attention, which hosts topological flat bands near Dirac point and exhibits remarkable interacting phases including correlated insulators, Chern insulators, and superconductor[27–29]. At the same time, the twisted-bilayer optical lattices based on ultracold atoms have been realized experimentally by our group[30]. This work takes a first step to study BEC and superfluid in the topological flat bands near Dirac point and the related rich interacting phases[31,32].

Online content

Any methods, additional references, Nature Portfolio reporting summaries, source data, extended data, supplementary information, acknowledgements, peer review information; details of author contributions and competing interests; and statements of data and code availability are available at https://doi.org/10.1038/s41566-025-01763-5.

References

1. Lv, B. Q., Qian, T. & Ding, H. Experimental perspective on three-dimensional topological semimetals. *Rev. Mod. Phys.* **93**, 025002 (2021).
2. Ong, N. P. & Liang, S. Experimental signatures of the chiral anomaly in Dirac-Weyl semimetals. *Nat. Rev. Phys.* **3**, 394–404 (2021).
3. Geim, A. K. & Novoselov, K. S. The rise of graphene. *Nat. Mater.* **6**, 183–191 (2007).
4. Castro Neto, A. H., Guinea, F., Peres, N. M. R., Novoselov, K. S. & Geim, A. K. The electronic properties of graphene. *Rev. Mod. Phys.* **81**, 109–162 (2009).
5. Schliemann, J., Loss, D. & Westervelt, R. M. Zitterbewegung of electronic wave packets in III-V zinc-blende semiconductor quantum wells. *Phys. Rev. Lett.* **94**, 206801 (2005).
6. Zhang, X. Observing Zitterbewegung for photons near the Dirac point of a two-dimensional photonic crystal. *Phys. Rev. Lett.* **100**, 113903 (2008).
7. Katsnelson, M. I., Novoselov, K. S. & Geim, A. K. Chiral tunnelling and the Klein paradox in graphene. *Nat. Phys.* **2**, 620–625 (2013).
8. Zhang, Y., Tan, Y. W., Stormer, H. L. & Kim, P. Experimental observation of the quantum Hall effect and Berry's phase in graphene. *Nature* **438**, 201–204 (2005).
9. Polini, M., Guinea, F., Lewenstein, M., Manoharan, H. C. & Pellegrini, V. Artificial honeycomb lattices for electrons, atoms and photons. *Nat. Nanotechnol.* **8**, 625–633 (2013).
10. Peleg, O. et al. Conical diffraction and gap solitons in honeycomb photonic lattices. *Phys. Rev. Lett.* **98**, 103901 (2007).
11. Song, D. et al. Controlled generation of pseudospin-mediated vortices in photonic graphene. *2D Mater.* **2**, 034007 (2015).
12. Song, D. et al. Unveiling pseudospin and angular momentum in photonic graphene. *Nat. Commun.* **6**, 6272 (2015).
13. Soltan-Panahi, P. et al. Multi-component quantum gases in spin-dependent hexagonal lattices. *Nat. Phys.* **7**, 434–440 (2011).

14. Tarruell, L., Greif, D., Uehlinger, T., Jotzu, G. & Esslinger, T. Creating, moving and merging Dirac points with a Fermi gas in a tunable honeycomb lattice. *Nature* **483**, 302–305 (2012).
15. Duca, L. et al. An Aharonov-Bohm interferometer for determining Bloch band topology. *Science* **347**, 288–292 (2015).
16. Li, T. et al. Bloch state tomography using Wilson lines. *Science* **352**, 1094–1097 (2016).
17. Brown, C. D. et al. Direct geometric probe of singularities in band structure. *Science* **377**, 1319–1322 (2022).
18. Fläschner, N. et al. Experimental reconstruction of the Berry curvature in a Floquet Bloch band. *Science* **352**, 1091–1094 (2016).
19. Weinberg, M., Staarmann, C., Ölschläger, C., Simonet, J. & Sengstock, K. Breaking inversion symmetry in a state-dependent honeycomb lattice: artificial graphene with tunable band gap. *2D Mater.* **3**, 024005 (2016).
20. Tarnowski, M. et al. Observation of topological Bloch-state defects and their merging transition. *Phys. Rev. Lett.* **118**, 240403 (2017).
21. Fläschner, N. et al. Observation of dynamical vortices after quenches in a system with topology. *Nat. Phys.* **14**, 265–268 (2018).
22. Tarnowski, M. et al. Measuring topology from dynamics by obtaining the Chern number from a linking number. *Nat. Commun.* **10**, 1728 (2019).
23. Wen, K. et al. Experimental study of tune-out wavelengths for spin-dependent optical lattice in ^{87}Rb Bose–Einstein condensation. *J. Opt. Soc. Am. B* **38**, 3269–3276 (2021).
24. Juzeliūnas, G., Ruseckas, J. & Dalibard, J. Generalized Rashba-Dresselhaus spin-orbit coupling for cold atoms. *Phys. Rev. A* **81**, 053403 (2010).
25. Campbell, D. L., Juzeliūnas, G. & Spielman, I. B. Realistic Rashba and Dresselhaus spin-orbit coupling for neutral atoms. *Phys. Rev. A* **84**, 025602 (2011).
26. Huang, L. et al. Experimental realization of two-dimensional synthetic spin-orbit coupling in ultracold Fermi gases. *Nat. Phys.* **12**, 540–544 (2016).
27. Cao, Y. et al. Unconventional superconductivity in magic-angle graphene superlattices. *Nature* **556**, 43–50 (2018).
28. Yankowitz, M. et al. Tuning superconductivity in twisted bilayer graphene. *Science* **363**, 1059–1064 (2019).
29. Lu, X. et al. Superconductors, orbital magnets and correlated states in magic-angle bilayer graphene. *Nature* **574**, 653–657 (2019).
30. Meng, Z. et al. Atomic Bose–Einstein condensate in twisted-bilayer optical lattices. *Nature* **615**, 231–236 (2023).
31. Julku, A., Bruun, G. M. & Törmä, P. Quantum geometry and flat band Bose-Einstein condensate. *Phys. Rev. Lett.* **127**, 170404 (2021).
32. Lukin, I., Sotnikov, A. & Kruchkov, A. Unconventional superfluidity and quantum geometry of topological bosons. Preprint at https://arxiv.org/abs/2307.08748 (2023).

Methods

A BEC of typical 5×10^5 atoms in $|F = 1, m_F = 1\rangle$ state is prepared in the crossed optical dipole trap. We load the 3D shaped BEC into a single layer of the 2D pancakes at maximum separation and then compress the pancake adiabatically to reach a deep 2D regime by an accordion lattice, as shown in Fig. 2a. The accordion lattice is formed by a 532 nm laser beam deflected by an acousto-optic deflector (AOD) and then split into two beams with variable spacing adjusted by the AOD. The two beams are focused onto the atoms with a 150 mm aspherical lens and interfere to form a standing wave in the vertical direction with variable separation. This separation can be varied from 12 µm down to 3 µm. We optimize it at $2\pi \times 1$ kHz to achieve superfluid of ultracold atoms. The 2D pancakes provide the strong confinement in z direction, which can apply balance forces to cancel or compensate the gravity. We use a far-red detuned 1064 nm laser propagating along the z direction to provide a harmonic trapping potential in x–y direction.

The optical honeycomb lattice is formed by three red-detuned laser beams operating at a wavelength $\lambda = 820$ nm. Each lattice beam is controlled by a single-pass acousto-optic modulators (AOM), which is used to change the frequency detuning between lattice beams. Then the three lattice beams are coupled into polarization-maintaining single-mode fibres respectively to improve the stability of the beam pointing and achieve better beam-profile quality. After the fibres, three lattice beams intersect at relative angles of 120° and interfere to create the optical honeycomb lattice potential. The lattice velocity $\mathbf{v}_i$ can be controlled by changing the detuning frequency of lattice beams $\mathbf{v}_i = a\Delta\omega_i\hat{k}_i$. Therefore, we can prepare BEC at the any quasi-momentum $\mathbf{q} = -m\mathbf{v}/\hbar$ in the lattice frame by choosing the appropriate linear combination of $\mathbf{v}_1$ and $\mathbf{v}_2$.

The ramp shapes of lattice beam intensity, detuning, harmonic trapping intensity in the x–y direction, and accordion lattice intensity are given in Fig. 2b. After creating a BEC, we load the 3D shaped BEC into a single layer of the 2D pancakes at maximum separation and then compress the pancake adiabatically to reach a deep 2D regime by an accordion lattice. Then we load the atoms into the lowest Bloch band at the Γ_0-point of the first Brillouin zone by adiabatically ramped up the honeycomb lattice. At the same time, the harmonic trapping potential is added in x–y direction. We transfer BEC adiabatically from Γ_0 to K_0, so the eigenstate $\Psi_s' = (1, 0)^T$ in the gauge transformed representation is prepared adiabatically with the help of the harmonic trapping potential in x–y direction. Finally, the harmonic trapping potential is ramped off quickly within 0.2 ms, followed by simultaneous switching off of the honeycomb lattice and accordion lattice. The atoms are detected by absorptive imaging with TOF of 18 ms to map the momentum components into the spatial density distribution of the BEC.

We transfer BEC from Γ_0 to K_0 with 0.8 ms and measure the atomic number of superfluid at Dirac point as function of waiting time. BEC at Dirac point has the limited lifetime with about several milliseconds since this state is not real ground state of the system as shown in Extended Data Fig. 1. For comparison, BEC at the Γ_0-point of the lowest Bloch band has long lifetime with more than one second.

In the experiment, we measure the contrast from the momentum-space diffraction peaks in the TOF images to determine the phase boundary between SF and MI. The phase boundary between SF and vortex is identified by checking if there is a quantized vortex of matter wave in the TOF images. We count the atoms in the different momentum regions to calculate the contrast, which is defined as $(n_{max} - n_{min})/(n_{max} + n_{min})$[33]. The vortex can be visually identified in the TOF images. The experimentally observed phase boundaries at Dirac point K_0 are shown in Fig. 4a, which are measured by choosing the several paths similar to the line (ii) with fixed harmonic trapping frequency and increasing lattice depths. First, we roughly determine the phase boundary by changing the lattice depths with the step of 1 E_R. This procedure only performs one measurement to obtain a rough phase boundary. Then we determine the phase boundary precisely by changing the lattice depths with the step of $0.2\,E_R$ near the rough phase boundary. Each point is based on three or more measurements and error bars are obtained to show the standard deviations of the mean. Using a similar method, we also measured the phase diagram at the M point, which includes only the conventional superfluid and Mott insulator phases, with a phase boundary that coincides with that of the K point, as shown in Extended Data Fig. 2.

Data availability

All data generated or analysed during this study are included in this published article. Additional data are also available from the corresponding authors upon reasonable request.

Code availability

The computer code used to generate the data supporting the findings of this study is available from the corresponding author upon reasonable request.

References

33. Gerbier, F. et al. Interference pattern and visibility of a Mott insulator. *Phys. Rev. A* **72**, 053606 (2005).

Acknowledgements

This research is supported by the National Key Research and Development Program of China (grant no. 2022YFA1404101), the Innovation Program for Quantum Science and Technology (grant no. 2021ZD0302003), National Natural Science Foundation of China (grant nos. 12488301, 12034011, U23A6004, 12322409, 12474252, 12474266 and 12374245), the Major Research Plan (High-precision Quantum Manipulation and Detection) of the National Natural Science Foundation of China, and Tencent (Xplorer Prize). C.C. acknowledges support by the National Science Foundation (grant no. PHY-2409612).

Author contributions

J.Z. conceived the idea and performed the experimental designs. Y.L., Z.M., W.Y. and J.Z. performed the experiments. C.C., W.H., Z.M., Y.L., W.Y. and J.Z. analysed the data and all authors discussed the results. W.H. and J.Z. performed the simulation. Z.M. plotted the figures. J.Z. and C.C. wrote the manuscript. All authors interpreted the results and reviewed the manuscript. J.Z. designed and supervised the project.

Competing interests

The authors declare no competing financial interests.

Additional information

Extended data is available for this paper at https://doi.org/10.1038/s41566-025-01763-5.

Supplementary information The online version contains supplementary material available at https://doi.org/10.1038/s41566-025-01763-5.

Correspondence and requests for materials should be addressed to Cheng Chin or Jing Zhang.

Peer review information *Nature Photonics* thanks the anonymous reviewers for their contribution to the peer review of this work.

https://doi.org/10.1038/s41566-025-01763-5

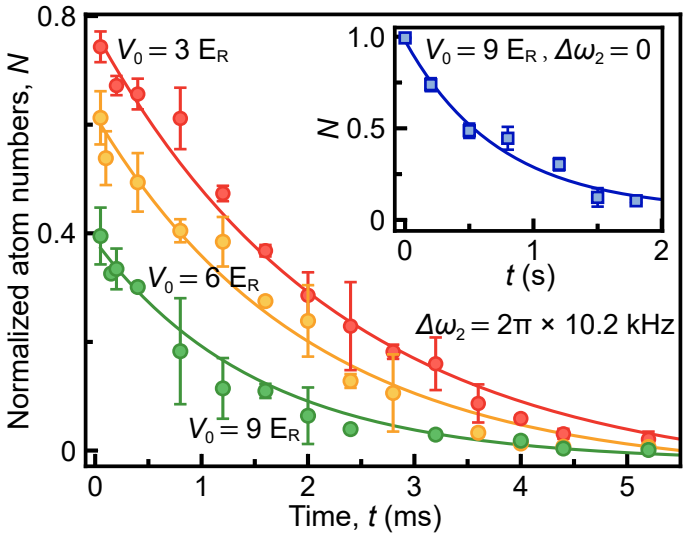

Extended Data Fig. 1 | The lifetime of BEC at Dirac point. The normalized atomic numbers of the superfluid component are plotted as function of waiting time at Dirac point for the different lattice depth. For comparison, the inset shows the data of the superfluid component as function of waiting time at the Γ_0-point of the lowest Bloch band. The points in the main and inset panels represent mean values from three and five independent measurements, respectively, and the error bars indicate standard deviations. Solid lines represent fits to the data using the mean values.

https://doi.org/10.1038/s41566-025-01763-5

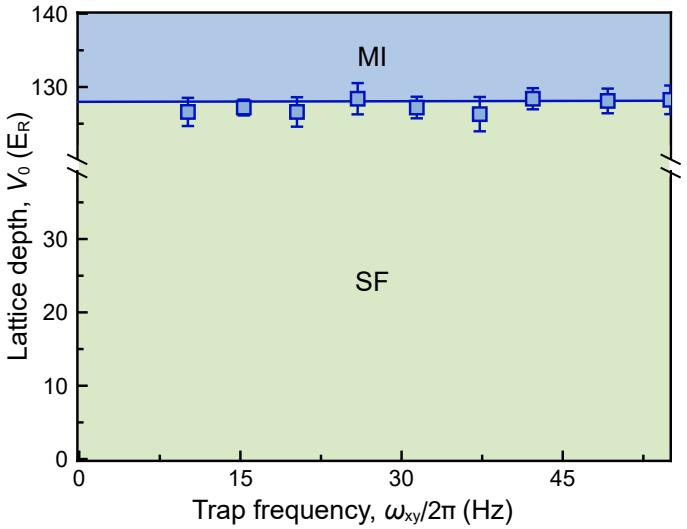

Extended Data Fig. 2 | Quantum phases at the M point of a honeycomb optical lattice for different trap frequencies ω_{xy} and lattice depths V_0. Here SF and MI refer to superfluid (green) and Mott insulator (blue), respectively. Each point represents the mean value from three independent measurements, and error bars represent the standard deviation of the measured phase boundary positions. The solid line shows a fit to the data using the mean values as reference.